

# **Tidal Disruption Events in Active Galactic Nuclei**

Chi-Ho Chan<sup>1,2</sup>, Tsvi Piran<sup>1</sup>, Julian H. Krolik<sup>3</sup>, and Dekel Saban<sup>1</sup>, Racah Institute of Physics, Hebrew University of Jerusalem, Jerusalem 91904, Israel

School of Physics and Astronomy, Tel Aviv University, Tel Aviv 69978, Israel

Department of Physics and Astronomy, Johns Hopkins University, Baltimore, MD 21218, USA Received 2019 April 27; revised 2019 June 18; accepted 2019 June 18; published 2019 August 20

#### **Abstract**

A fraction of tidal disruption events (TDEs) occur in active galactic nuclei (AGNs) whose black holes possess accretion disks; these TDEs can be confused with common AGN flares. The disruption itself is unaffected by the disk, but the evolution of the bound debris stream is modified by its collision with the disk when it returns to pericenter. The outcome of the collision is largely determined by the ratio of the stream mass current to the azimuthal mass current of the disk rotating underneath the stream footprint, which in turns depends on the mass and luminosity of the AGN. To characterize TDEs in AGNs, we simulated a suite of stream—disk collisions with various mass current ratios. The collision excites shocks in the disk, leading to inflow and energy dissipation orders of magnitude above Eddington; however, much of the radiation is trapped in the inflow and advected into the black hole, so the actual bolometric luminosity may be closer to Eddington. The emergent spectrum may not be thermal, TDE-like, or AGN-like. The rapid inflow causes the disk interior to the impact point to be depleted within a fraction of the mass return time. If the stream is heavy enough to penetrate the disk, part of the outgoing material eventually hits the disk again, dissipating its kinetic energy in the second collision; another part becomes unbound, emitting synchrotron radiation as it shocks with surrounding gas.

Key words: accretion, accretion disks – black hole physics – galaxies: nuclei – hydrodynamics – methods: numerical

#### 1. Introduction

A tidal disruption event (TDE) occurs when a star wanders within the tidal radius of a black hole and is ripped apart by tidal gravity; roughly half of the star is expelled as unbound debris while the other half remains bound on highly eccentric orbits. In the standard picture, general relativistic effects cause the bound debris orbits to precess and self-intersect. Shocks at the intersections dissipate kinetic energy, and the stream of bound debris is promptly gathered into an accretion disk with radius approximately twice the stream pericenter distance (e.g., Rees 1988). However, unless the stream pericenter is within  $\sim$ 10 gravitational radii of the black hole, general relativistic precession creates only weak, oblique shocks near apocenter that dissipate energy inefficiently (Dai et al. 2015; Shiokawa et al. 2015). Consequently, the disk may not form right away, and most of the stream will return to large distances. These weak shocks could be responsible for the emission in optical TDEs (Piran et al. 2015).

This picture tacitly assumes that TDEs happen in vacuum. However, the black hole in an active galactic nucleus (AGN) is surrounded by an accretion disk. As a star heads toward the black hole on a trajectory destined for tidal disruption, its initial passage through the disk leaves no lasting impact on either the star or the disk because the density contrast between the two is immense. But after the star is tidally disrupted, the bound debris stream has such a low density that, when it returns to pericenter, it can interact with the disk in a more interesting manner (Kochanek 1994; see also Kathirgamaraju et al. 2017). The collision between the stream and the disk can potentially dissipate much of the kinetic energy possessed by the stream and the disk gas near the impact point, which can be radiated away. The collision can also alter the subsequent evolution of the stream and drastically damage the disk. The collision with the disk likely produces a brighter signal and has a greater

effect on the stream than any other interaction with circumnuclear material (Bonnerot et al. 2016) because the disk is far denser.

Several percent of galaxies harbor AGNs, so a similar fraction of TDEs should take place in AGN hosts. This number is made uncertain to the degree that the distribution of stellar orbits near an AGN is systematically different from the center of an inactive galaxy, and that the black hole in a galaxy with an AGN tends to be more massive than a galaxy without one (see also Karas & Šubr 2007; Kennedy et al. 2016). Because both TDEs and AGNs vary on timescales of weeks to months, and because a TDE in an AGN presents less contrast against the prior state of the system than a TDE in an inactive galaxy, deciding whether an increase in brightness is due to a TDE or is merely AGN variability is not trivial (Komossa 2015; Kankare et al. 2017; Auchettl et al. 2018; Trakhtenbrot et al. 2019b); indeed, there are a number of cases in which the correct identification of a particular episode of variation is disputed (e.g., Campana et al. 2015; Grupe et al. 2015; Merloni et al. 2015; Saxton et al. 2015; Blanchard et al. 2017; Lin et al. 2017; Wyrzykowski et al. 2017; Mattila et al. 2018; Shu et al. 2018). It is therefore of interest to see if TDEs in AGNs have distinctive observational characteristics that allow us to recognize them more reliably.

Numerous physical processes interact in the course of these events. Radiation is expected to contribute significantly to the internal energy in the parts of the disk affected by the collision, while magnetohydrodynamics (MHD) is critical to both radial inflow and, at higher altitudes, vertical support. Consequently, a proper study of the collision calls for simulations including both general relativistic MHD and the interaction between gas and radiation. Moreover, the collision is described by a number of parameters: the black hole mass, the stellar mass, the disk accretion rate, and the orientation of the stream with respect to

the disk. A large suite of simulations covering the realizable subset of the multidimensional parameter space is needed to probe the full range of observational behavior. As an exploratory step, here we present pure-hydrodynamics simulations of one particular configuration of the collision. Our simulations consider only the portion of the event when the mass return rate is maximum, and they focus on the dependence on one parameter, the ratio of the stream mass current to the azimuthal mass current of the disk passing under the stream footprint. Nonetheless, even these simulations identify a number of key mechanisms and reveal the principal issues that must be resolved before making definite observational predictions.

We start off by estimating the properties of stream-disk collisions in Section 2. We introduce our simulation setup in Section 3, present our results in Section 4 (see movie), and discuss possible observational signatures in Section 5. Our conclusions are summarized in Section 6.

### 2. Analytic Considerations

A star of mass  $M_{\star}$  and radius  $r_{\star}$  is torn apart when it flies by a black hole of mass  $M_h$  on an orbit whose pericenter distance  $r_{\rm p}$  is smaller than the tidal radius  $r_{\rm t} \equiv r_{\star} (M_{\star}/M_{\rm h})^{-1/3}$ (Hills 1975). The tidal radius for a main-sequence star interacting with a black hole commonly found in galactic nuclei is only several tens of gravitational radii  $r_g \equiv GM_h/c^2$  of the black hole, where G is the gravitational constant and c is the speed of light:

$$\frac{r_{\rm t}}{r_{\rm g}} \approx 50 \left(\frac{M_{\rm h}}{10^6 M_{\odot}}\right)^{-2/3} \left(\frac{M_{\star}}{M_{\odot}}\right)^{-1/3} \left(\frac{r_{\star}}{R_{\odot}}\right). \tag{1}$$

The portion of the debris remaining bound to the black hole traverses a highly elliptical orbit and returns to pericenter as a stream. Different parts of the stream have different semimajor axes; the part with semimajor axis a returns to pericenter at time  $T = 2\pi (GM_h/a^3)^{-1/2}$  after disruption. The most bound part has the smallest semimajor axis  $a_{\rm mb} \sim \frac{1}{2} r_{\rm p}^2 / r_{\star}$  and returns to pericenter soonest, after a mass return time of

$$T_{\rm mb} \sim \frac{\pi}{\sqrt{2}} \left(\frac{GM_{\rm h}}{r_{\rm p}^3}\right)^{-1/2} \left(\frac{M_{\star}}{M_{\rm h}}\right)^{-1/2} \left(\frac{r_{\rm p}}{r_{\rm t}}\right)^{3/2}.$$
 (2)

If the bound mass is uniformly distributed in specific binding energy  $E = GM_h/(2a)$ , that is,  $dM_{\star}/dE \sim \frac{1}{2}M_{\star}/(GM_h r_{\star}/r_p^2)$ , the stream mass current, or the peak rate at which mass returns to pericenter at early times, is

$$\begin{split} \dot{M}_{\rm S} \sim & \left[ \frac{dM_{\star}}{dE} \left| \frac{dE}{da} \right| \frac{da}{dT} \right]_{a=a_{\rm mb}} \\ \sim & \frac{\sqrt{2}}{3\pi} M_{\star} \left( \frac{GM_{\rm h}}{r_{\rm p}^3} \right)^{1/2} \left( \frac{M_{\star}}{M_{\rm h}} \right)^{1/2} \left( \frac{r_{\rm p}}{r_{\rm t}} \right)^{-3/2}. \end{split} \tag{3}$$

Note that  $\dot{M}_{\rm s}T_{\rm mb}\sim \frac{1}{3}M_{\star}$ . The black hole of an AGN has an accretion disk prior to the TDE. The stream intersects the disk at two points, the line joining which passes through the black hole as well. Because stars originate from all directions, this line is randomly oriented in the stream plane. Moreover, because the apocenter of a highly eccentric orbit subtends only a small angle at the black hole, the stream crosses the disk near pericenter much more often than near apocenter. The configuration considered by Kathirgamaraju et al. (2017), in which the stream travels within a thick, very weakly accreting disk and interaction occurs most strongly near apocenter, is special in comparison (see also Blanchard et al. 2017). For simplicity, we consider a parabolic stream slamming perpendicularly into the disk at pericenter.

The stream interacts with the azimuthal mass current of the disk rotating underneath its footprint, given by

$$\dot{M}_{\rm d} \sim 4R_{\rm s}\Sigma_{\rm d} \left(\frac{GM_{\rm h}}{r_{\rm p}}\right)^{1/2},$$
 (4)

where  $R_s$  is the stream width at pericenter and  $\Sigma_d$  is the disk surface density at stream pericenter measured from the midplane to infinity. A wider stream results in a larger  $\dot{M}_{\rm d}$ , but  $\dot{M}_{\rm s}$  is unchanged because it is determined purely by orbital dynamics. The disk accretion rate,

$$\dot{M}_{\rm a} \sim 2\pi r_{\rm p}^2 \Sigma_{\rm d} \alpha (H/R)_{\rm d}^2 \left(\frac{GM_{\rm h}}{r_{\rm p}^3}\right)^{1/2},$$
 (5)

with  $\alpha$  the Shakura & Sunyaev (1973) parameter and  $(H/R)_d$ the disk aspect ratio at stream pericenter, is much smaller

The ratio  $\dot{M}_{\rm s}/\dot{M}_{\rm d}$  is the most important quantity governing the outcome of the collision, and it is the parameter we vary in our simulations. We would like to relate  $\dot{M}_{\rm s}/\dot{M}_{\rm d}$  to the observables  $M_h$  and  $L_a$ ; here  $L_a = \eta \dot{M}_a c^2$  is the disk accretion luminosity and  $\eta$  is the accretion efficiency. The value of  $\dot{M}_{\rm d}$ depends on the conditions of the disk. For typical TDEs in AGNs, electron scattering dominates opacity in a Shakura & Sunyaev (1973) disk at stream pericenter. The nature of pressure switches from gas to radiation when

$$\frac{L_{\rm a}}{L_{\rm E}} \gtrsim 0.004 \left(\frac{M_{\rm h}}{10^6 M_{\odot}}\right)^{-1} \left(\frac{M_{\star}}{M_{\odot}}\right)^{-7/16} \\
\times \left(\frac{r_{\star}}{R_{\odot}} \frac{r_{\rm p}}{r_{\rm l}}\right)^{21/16} \left(\frac{\alpha}{0.1}\right)^{-1/8} \left(\frac{\eta}{0.1}\right), \tag{6}$$

where  $L_{\rm E} = 4\pi G M_{\rm h} c / \kappa_{\rm T}$  is the Eddington luminosity and  $\kappa_{\rm T}$ is the cross section per mass for Thomson scattering. Now  $\dot{M}_{\rm d}/\dot{M}_{\rm a} \propto (H/R)_{\rm d}^{-2}$ , and  $(H/R)_{\rm d} \propto \dot{M}_{\rm a}^{1/5}$  and  $(H/R)_{\rm d} \propto \dot{M}_{\rm a}$  for gas- and radiation-dominated disks respectively; therefore,  $\dot{M}_{
m d}$  increases with  $L_{
m a}/L_{
m E}$  in a gas-dominated disk, then decreases with  $L_{\rm a}/L_{\rm E}$  as the disk becomes radiationdominated.

Figure 1 shows the dependence of  $\dot{M}_{\rm s}/\dot{M}_{\rm d}$  on  $M_{\rm h}$  and  $L_{\rm a}/L_{\rm E}$ . Holding  $M_h$  constant, a given level of  $M_s/M_d$  can be realized in either a weakly accreting, gas-dominated disk or a strongly accreting, radiation-dominated disk. The value of  $\dot{M}_{\rm s}/\dot{M}_{\rm d}$  tends to stay above unity, dipping below only for the dimmest and most massive AGNs; this is fortuitous because a number of our simulation results (Figures 5, 6, 8, 9, and 11) depend weakly on  $\dot{M}_{\rm s}/\dot{M}_{\rm d}$  once it is large enough.

We can estimate time-integrated consequences of the collision by comparing global measures of stream and disk

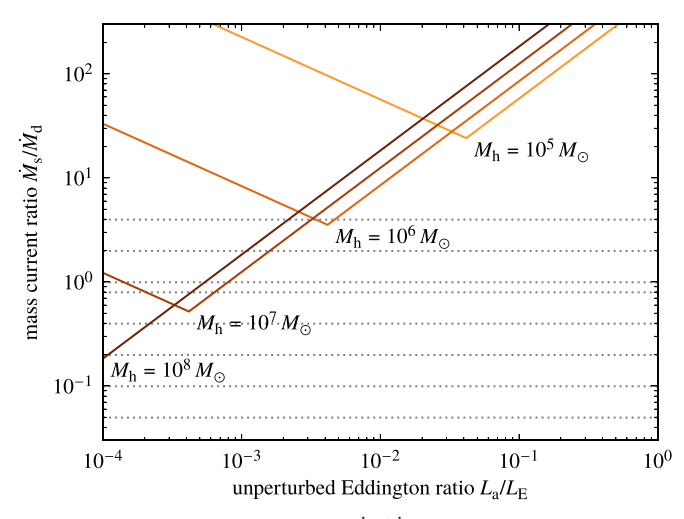


**Figure 1.** Plot of the mass current ratio  $\dot{M}_{\rm s}/\dot{M}_{\rm d}$  as a function of the black hole mass  $M_{\rm h}$  and the unperturbed disk Eddington ratio  $L_{\rm a}/L_{\rm E}$  for our fiducial parameters  $M_{\star}=M_{\odot},\ r_{\star}=R_{\odot},\ r_{\rm p}=r_{\rm t},\ R_{\rm s}=r_{\star},\ \alpha=0.1,\ {\rm and}\ \eta=0.1$  (Section 3.3). Solid lines reach a minimum when pressure in the disk shifts from gas-dominated on the left to radiation-dominated on the right. The horizontal lines are the  $\dot{M}_{\rm s}/\dot{M}_{\rm d}$  used in our simulations (Section 3.4).

physical quantities. The mass ratio is

$$\frac{\frac{1}{2}M_{\star}}{2\pi r_{\rm p}^{2}\Sigma_{\rm d}} \sim 80 \left(\frac{M_{\rm h}}{10^{6}M_{\odot}}\right)^{-1} \left(\frac{M_{\star}}{M_{\odot}}\right)^{3/2} \left(\frac{r_{\star}}{R_{\odot}}\frac{r_{\rm p}}{r_{\rm i}}\right)^{-3/2} \times \left(\frac{L_{\rm a}/L_{\rm E}}{0.005}\right)^{-1} \left(\frac{\alpha}{0.1}\right) \left(\frac{\eta}{0.1}\right) \left[\frac{(H/R)_{\rm d}}{0.003}\right]^{2}.$$
(7)

Because the stream velocity at pericenter is  $\sqrt{2}$  times the disk orbital velocity there, the momentum ratio is of the same order as the mass ratio. This means the stream carries enough mass and momentum to potentially reshape and reorient the disk. Similarly, the ratio of stream kinetic energy to disk binding energy is of order the mass ratio; therefore, if all the stream kinetic energy were dissipated, the stream could heat the disk sufficiently to unbind it.

If the dissipated energy were instead radiated away immediately, the collision could be quite luminous:

$$\frac{\dot{M}_{\rm s}(GM_{\rm h}/r_{\rm p})}{L_{\rm E}} \sim 30 \left(\frac{M_{\rm h}}{10^6 M_{\odot}}\right)^{-5/6} \times \left(\frac{M_{\star}}{M_{\odot}}\right)^{7/3} \left(\frac{r_{\star}}{R_{\odot}}\right)^{-5/2} \left(\frac{r_{\rm p}}{r_{\rm i}}\right)^{-4}, \tag{8}$$

corresponding to  $\dot{M}_{\rm s}(GM_{\rm h}/r_{\rm p})/L_{\rm a}\approx 6000$  for a disk with  $L_{\rm a}/L_{\rm E}\approx 0.005$ . We shall discuss in Section 5.3.2 why the actual luminosity could be very different.

### 3. Methods

The stream—disk collision is simulated with Athena++, a rewrite of the finite-volume hydrodynamics code Athena (Stone et al. 2008). We adopt the cylindrical coordinates  $(R, \phi, z)$ . Due to the coordinate singularity at R=0, we must restrict the lower-radial boundary of our simulation domain to R>0, thus introducing a cylindrical cutout in the center of our simulation domain. Gas directed toward the cutout is removed from the simulation entirely. Other details of our numerical setup follow.

### 3.1. Equations

The stream pericenter distance of typical TDEs is only tens of  $r_{\rm g}$  (Section 2). Given other approximations used, it is reasonable to neglect relativistic effects. The hydrodynamics equations are

$$\frac{\partial \rho}{\partial t} + \nabla \cdot (\rho \mathbf{v}) = 0, \tag{9}$$

$$\frac{\partial}{\partial t}(\rho \mathbf{v}) + \nabla \cdot (\rho \mathbf{v} \mathbf{v} + p \mathbf{I}) = -\rho \nabla \Phi, \tag{10}$$

$$\frac{\partial E}{\partial t} + \nabla \cdot [(E+p)v] = -\rho v \cdot \nabla \Phi. \tag{11}$$

Here  $\rho$ ,  $\nu$ , and p are density, velocity, and pressure,  $\Phi(R,z) = -GM_{\rm h}/(R^2+z^2)^{1/2}$  is the gravitational potential of the black hole, and I is the isotropic rank-two tensor. We use an adiabatic equation of state. The total energy is  $E=\frac{1}{2}\rho v^2+\rho e$ , where  $\rho e=p/(\gamma-1)$  is the internal energy. Disk pressure can be dominated by gas or radiation (Section 2); for simplicity, we choose the adiabatic index to be  $\gamma=\frac{5}{3}$ . As we shall see later in Section 5.3.1, the thermodynamic conditions of a realistic disk is likely more complicated than a simple choice between gas and radiation pressure.

### 3.2. Code Units

Simulation quantities are expressed in code units of length  $r_0$ , time  $\Omega_0^{-1} \equiv (GM_{\rm h}/r_0^3)^{-1/2}$ , velocity  $v_0 \equiv r_0\Omega_0$ , and density  $\rho_0$ . Because Newtonian gravity, unlike relativistic gravity, is scale-free, the dimensionless versions of Equations (9)–(11) in this unit system are independent of  $r_0$  and  $\rho_0$ . With an appropriate choice of these two quantities, our results can be scaled to the conditions of any particular TDE.

We set  $r_0 = r_p$ , the characteristic length scale of the system. Time is reported as the number of disk orbits at  $R = r_0$ , or disk orbits for short; one disk orbit is  $2\pi (r_p/r_t)^{3/2}$  times the stellar dynamical time. The mass return time in Equation (2) is

$$T_{\rm mb} \sim 400 \left(\frac{M_{\rm h}}{10^6 M_{\odot}}\right)^{1/2} \left(\frac{M_{\star}}{M_{\odot}}\right)^{-1/2} \times \left(\frac{r_{\rm p}}{r_{\rm t}}\right)^{3/2} {\rm disk~orbits}.$$
 (12)

The value of  $\rho_0$  will be determined in Section 3.5.

### 3.3. Fiducial Parameters

When translating simulation results from code units to physical units, we adopt the same fiducial parameters as in Section 2, to wit,  $M_{\rm h}=10^6M_{\odot}$ ,  $M_{\star}=M_{\odot}$ ,  $r_{\star}=R_{\odot}$ ,  $r_{\rm p}=r_{\rm t}$ ,  $R_{\rm s}=r_{\star}$ ,  $\alpha=0.1$ , and  $\eta=0.1$ .

### 3.4. Stream and Disk Properties

The initial disk has a constant midplane density  $\rho_0$  and a Gaussian scale height  $\propto R$ :

$$\rho(R, z) = \rho_0 \exp[-\Delta \Phi / (\mathcal{H}^2 v_K^2)]. \tag{13}$$

Here  $\Delta\Phi(R,z) \equiv \Phi(R,z) - \Phi(R,0)$  is the gravitational potential difference from the midplane and is  $\approx \frac{1}{2}v_{\rm K}^2(z/R)^2$  for our spherically symmetric  $\Phi$ , where  $v_{\rm K}^2(R) \equiv (\partial\Phi/\partial \ln R)_{z=0}$  is the square of the midplane Keplerian orbital velocity. The

aspect ratio of the simulated disk is  $\mathcal{H}=0.1$ ; it is much larger than the aspect ratio of a Shakura & Sunyaev (1973) disk for numerical reasons, and the effect of this choice will be considered in Section 3.5. The pressure of the disk is  $p(R, z) = \rho \mathcal{H}^2 v_K^2$ . Its orbital velocity, given by

$$v_{\phi}^{2}(R,z) = v_{K}^{2} + (\Delta\Phi + \mathcal{H}^{2}v_{K}^{2})(\partial \ln v_{K}^{2}/\partial \ln R), \qquad (14)$$

is slightly sub-Keplerian to counteract pressure forces.

Our initial disk is not a Shakura & Sunyaev (1973) disk. For example, its surface density profile is

$$\Sigma(R) = \int_0^{z_{\text{max}}} dz \, \rho \approx \left(\frac{1}{2}\pi\right)^{1/2} \mathcal{H}\rho_0 R,\tag{15}$$

where  $z_{\rm max}$  is the distance of the vertical boundaries of the simulation domain from the midplane. This surface density profile is neither the  $\Sigma \propto R^{-3/5}$  profile of a gas-dominated disk nor the  $\Sigma \propto R^{3/2}$  profile of a radiation-dominated disk, although it is close to the latter. The advantage of our initial disk is that it is scale-free, so we can scale our results to fit any TDE of interest. As long as we pick  $\rho_0$  such that  $\dot{M}_{\rm s}/\dot{M}_{\rm d}$  is the same for our initial disk and for a Shakura & Sunyaev (1973) disk, our results are not qualitatively affected.

Ideally, we would like our stream to travel on a parabolic trajectory vertical to the midplane: The stream would approach pericenter from  $\phi = \pi$ , cross the axis, reach pericenter at  $(R, \phi, z) = (r_0, 0, 0)$ , and return to infinity along  $\phi = \pi$ . Unfortunately, the trajectory would then cross the cylindrical cutout in the center of the simulation domain. We solve this problem in two ways. For lighter streams that are effectively stopped by the disk, we can simply lower the upper-vertical boundary of the simulation domain until the stream intersects the boundary at  $\phi = 0$ ; if the stream is injected as a boundary condition from the intersection, it will not encounter the cutout before it terminates at pericenter. For heavier streams that can punch through the disk, we additionally rotate the trajectory 0.15 rad from the vertical to make it avoid the cutout altogether. The sense of the rotation is to make the trajectory prograde with respect to the disk, increasing the likelihood that the outgoing material will miss the cutout. Since the vertical and inclined streams differ so little in inclination, we treat them as directly comparable. We leave the exploration of streams of other spatial orientations to future work.

We choose the stream boundary condition so that, if the stream traveled ballistically to pericenter, its cross section there would be circular and its transverse density profile would be a Gaussian of radius  $Wr_0$ , where W=0.02. The simulated stream width is slightly wider than in typical TDEs. The density at the center of the Gaussian is set by matching the desired value of  $\dot{M}_{\rm s}$ , and the pressure is  $10^{-6} \, v_0^2$  times density. Tracing orbits back to the upper-vertical boundary determines the stream density, velocity, and pressure there.

The disk mass current is  $\dot{M}_{\rm d} \approx 0.01 \; \rho_0 r_0^2 v_0$ . We use  $\dot{M}_{\rm s} \in \{0.5, 1, 2, 4, 8\} \times 10^{-3} \; \rho_0 r_0^2 v_0$  for the vertical stream and  $\dot{M}_{\rm s} \in \{1, 2, 4\} \times 10^{-2} \; \rho_0 r_0^2 v_0$  for the inclined stream. Altogether, we have  $\dot{M}_{\rm s}/\dot{M}_{\rm d} \in \{\approx 0.05, \approx 0.1, \approx 0.2, \approx 0.4, \approx 0.8, \approx 1, \approx 2, \approx 4\}$ . Combinations of  $M_{\rm h}$  and  $L_{\rm a}$  giving such  $\dot{M}_{\rm s}/\dot{M}_{\rm d}$  can be read off from Figure 1. Only the heaviest stream pertains to our fiducial parameters (Section 3.3); the lighter streams are also valid if  $M_{\rm h}$  is larger or  $\alpha$  is smaller.

The initial disk and the stream have respectively  $|j| \lesssim 0.2 \, r_0 v_0$  and  $j \gtrsim 1.4 \, r_0 v_0$ , where j is the specific angular momentum in the  $\phi = \frac{1}{2}\pi$  direction. For the purpose of separating disk-like gas from stream-like gas when analyzing our results in Section 4, we adopt the conservative cutoff  $j = 1.1 \, r_0 v_0$ .

### 3.5. Stream and Disk Density

The aspect ratio of a Shakura & Sunyaev (1973) disk at stream pericenter,  $(H/R)_{\rm d} \sim 0.003$ , and the stream width,  $R_{\rm s} \sim r_{\star}$ , are both difficult to resolve spatially; this is why the simulated disk height and stream width are artificially increased to  $\mathcal{H}r_0$  and  $\mathcal{W}r_0$  respectively, with  $\mathcal{H}=0.1$  and  $\mathcal{W}=0.02$  (Section 3.4). To preserve the mass currents under such a modification, we simultaneously adjust the midplane density of the disk and the central density of the stream. We demand that the simulated disk mass current,  $4\mathcal{W}r_0\Sigma(r_0)\nu_0$ , be equal to  $\dot{M}_{\rm d}$  of a realistic disk. This, together with Equations (3) and (15), yields

$$\rho_0 = \frac{1}{6\pi^{3/2} \mathcal{HW}} \frac{M_{\star}}{r_{\star}^3} \left(\frac{M_{\star}}{M_{\rm h}}\right)^{3/2} \left(\frac{r_{\rm p}}{r_{\rm t}}\right)^{-9/2} (\dot{M}_{\rm s}/\dot{M}_{\rm d})^{-1}.$$
 (16)

Similarly, the central density of the stream is determined by matching the desired  $\dot{M}_{\rm s}$ . Because the mass currents involved in the collision are independent of the particular values of  $\mathcal{H}$  and  $\mathcal{W}$  provided both are  $\ll 1$ , the outcome of the collision should not be severely affected by our choices for these quantities. Volume-integrated quantities in our simulations, such as the inflow rate (Section 4.2.2) and the energy dissipation rate (Section 4.3), are likewise genuine. Although the simulated disk is unrealistically thick at the beginning, any structure created in the course of the simulations with aspect ratio  $\gg \mathcal{H}$  is realistic because its thickness is due to the injection of internal energy much greater than the artificial internal energy in the initial condition.

### 3.6. Other Numerical Considerations

Periodic boundary conditions are used for the azimuthal direction. Outflow boundary conditions are used for the radial and vertical directions: Velocity is copied from the last physical cell into the ghost zone and inward-pointing velocity components are zeroed, while density and pressure are isothermally extrapolated such that the pressure gradient balances gravitational and centrifugal forces in the ghost zone. On the uppervertical boundary, the stream injection condition (Section 3.4) supersedes this boundary condition wherever the former predicts a larger density.

The numerical vacuum is an axisymmetric hydrostatic torus. Its density is determined by the constraint

constant = 
$$-\Phi(R, z) + \frac{(\nu_{\phi}^2)_{\text{v}}}{2 - 2q} - K \frac{\Gamma}{\Gamma - 1} \rho_{\text{v}}^{\Gamma - 1},$$
 (17)

its velocity is  $\mathbf{v}_{\rm v} = v_0 (R/r_0)^{1-q} \, \hat{\mathbf{e}}_{\phi}$ , and its pressure is  $p_{\rm v} = K \rho_{\rm v}^{\Gamma}$ . The parameters in these equations are q = 1.75,  $K = 0.5 \, \rho_0^{1-\Gamma} \, v_0^2$ , and  $\Gamma = 0.9$ ; the constant on the left-hand side of Equation (17) follows from requiring that  $\rho_{\rm v}$  attain a

maximum of  $10^{-6}\rho_0$  at  $(R,z)=(r_0,0)$ . As the simulation progresses, we keep the density and pressure of every cell greater than or equal to its vacuum value at all times. In addition, whenever the density of a cell drops to  $0 < \xi < 1$  times vacuum, we simultaneously modify its velocity to  $\xi v + (1 - \xi)v_v$  so as to prevent velocities from erroneously growing in low-density regions.

The simulation domain spans  $[0.15 \ r_0, 5 \ r_0] \times [-\pi, \pi] \times [-3.2 \ r_0, 1.6 \ r_0]$  in  $(R, \phi, z)$ . The inner-radial boundary at  $R = 0.15 \ r_0$  encloses a cylindrical cutout in the center of the simulation domain, introduced to exclude the coordinate singularity at R = 0. The radius of the cutout in physical units is  $\approx 7 \ r_{\rm g} \ [M_{\rm h}/(10^6 M_\odot)]^{-2/3} (M_\star/M_\odot)^{-1/3} (r_\star/R_\odot) (r_{\rm p}/r_{\rm t})$ , which is just outside the innermost stable circular orbit of a nonrotating black hole; therefore, we are simulating the entire disk interior to the stream pericenter, and we may regard gas entering the cutout as falling into the black hole. The lower-vertical boundary is twice as far below the midplane as the upper-vertical boundary so that we can follow as much of the gas leaving the lower side of the disk as feasible.

The number of grid cells is  $200 \times 200 \times 300$ . We employ a power-law grid in the radial direction for which  $\Delta R_{i+1}/\Delta R_i=1.01$ ; this policy gives us cells with approximately square poloidal cross sections at  $R=r_0$ . The pressure scale height of the disk at stream pericenter,  $\approx \sqrt{2} \, \mathcal{H} r_0$ , is resolved with around nine vertical cells, and the stream width,  $\mathcal{W} r_0$ , is barely resolved with around two azimuthal cells at the injection point.

The simulations run to 100 disk orbits which, according to Equation (12), is  $\sim 0.3 T_{\rm mb} [M_{\rm h}/(10^6 M_{\odot})]^{-1/2} (M_{\star}/M_{\odot})^{1/2} (r_{\rm p}/r_{\rm t})^{-3/2}$ . This means our simulations focus on the time when the mass return rate is greatest, and the mass return rate varies little over the course of our simulations.

#### 4. Results

# 4.1. Overview

We use the  $\dot{M}_{\rm s}/\dot{M}_{\rm d}\approx 0.2$  simulation to illustrate how the disk in any simulation evolves in general (see movie). The left column of Figure 2 displays an early time, 10 disk orbits. The incoming stream is visible above the disk in the poloidal slice. The vertical structure near the center of the cylindrical slice is the part of the stream closest to pericenter; it is bent because the disk deflects the stream in the direction of disk rotation. The stream opens an annular gap in the disk at  $R\approx r_0$ , manifest in the poloidal and midplane slices; the gap separates the inner disk (Section 4.2) at  $R\leqslant r_0$  from the outer disk.

Nonaxisymmetric features appear in the midplane slice. The most salient one is the curved bow shock with its tip at  $(R, \phi) \approx (r_0, 0.1\pi)$ ; here  $\phi > 0$  because of stream deflection. The inner half of the bow shock extends inward, forming a prominent spiral shock in the inner disk. There are typically multiple spiral shocks; together, they drive an extremely powerful inflow that is orders of magnitude stronger than in the unperturbed disk (Section 4.2.1).

Nonaxisymmetric features in the outer disk can be understood with the help of the cylindrical slice. The incoming stream pushes stream and disk gas out of the other side of the disk. Part of this gas reaches as far as  $z \approx -r_0$  before gravity pulls it back down to strike the disk at  $\phi \approx -\frac{3}{4}\pi$ ; the impact compresses the disk and launches a spiral shock stretching outward from  $(R, \phi) \approx (1.2 \, r_0, 0.8\pi)$ . The impacting gas

glances off the disk and falls back to it once again at  $\phi \approx \frac{3}{8}\pi$ , launching another, much weaker, spiral feature. At the time shown, the weak spiral feature is hidden from view by the similarly located and much stronger bow shock, but it becomes more conspicuous at late times when the bow shock is weaker. Both spiral features are stationary in space.

The center column depicts an intermediate time, 25 disk orbits. The gap widens and the spiral shocks deplete the inner disk, as evidenced by the poloidal and midplane slices. The reduction of disk gas at  $R \lesssim 1.2~r_0$  is the reason why the stream suffers less deflection in the cylindrical slice. The collision heats the inner disk, causing its gas to puff up and move to larger radii, easily seen by comparing the poloidal slices of early and intermediate times.

The intermediate time is taken during an episode of disk evolution in which the outer edge of the gap, as witnessed in the midplane slice, becomes highly nonaxisymmetric; as the outer edge orbits around, acoustic waves are sent propagating outward at the same frequency as its orbital frequency. These waves have large enough amplitudes to obscure the spiral features in the outer disk.

The right column presents a late time, 65 disk orbits. The inner disk is largely cleared out; as a result, spiral shocks in the inner disk are barely visible. The outer edge of the cavity returns to approximate axisymmetry, so waves are no longer launched and the two spiral features in the outer disk remerge. The spiral shock extending outward from  $(R, \phi) \approx (1.5 \ r_0, 0.8\pi)$  remains well-defined, but the weak spiral feature starting from  $(R, \phi) \approx (2.6 \ r_0, 0.4\pi)$  is merely a diffuse density enhancement. The outer half of the bow shock appears as a spur joining the weak spiral feature.

The incoming stream in the  $\dot{M}_{\rm s}/\dot{M}_{\rm d}\approx 0.2$  simulation is not heavy enough to produce a perceptible stream of outgoing material (Section 4.4); for a better view of the outgoing material, we turn to the  $\dot{M}_{\rm s}/\dot{M}_{\rm d}\approx 1$  simulation. The slices shown in Figure 3 roughly follow the orbital plane of the outgoing material. The outgoing material exits the disk not as a dense, collimated structure, but as a clumpy plume orders of magnitude more dilute than the incoming stream. The plume is more spread out in the orbital plane than perpendicular to it.

### 4.2. Inner Disk

# 4.2.1. Dynamics

Figure 4 displays three snapshots from three simulations. The snapshots are selected from early times when the inner disk is still largely intact, but our comments below hold for all simulations at all times. At the times shown, the stream has delivered the same amount of mass, momentum, and energy across all simulations.

The top row demonstrates how the collision excites spiral shocks in the inner disk. Spiral shocks vary in number, position, and strength over time, but there is often a dominant pair, one connected to the bow shock, the other located almost directly opposite in the other half of the inner disk. The former spiral shock is typically stronger and is marked with black arcs in the figure.

Spiral shocks deflect orbiting gas. The stronger spiral shock tends to deflect gas inward, giving rise to a region of inward mass flux immediately after the shock in the middle row. The net effect of the multiple spiral shocks is to remove angular momentum from the orbiting gas; as a result, gas falls toward

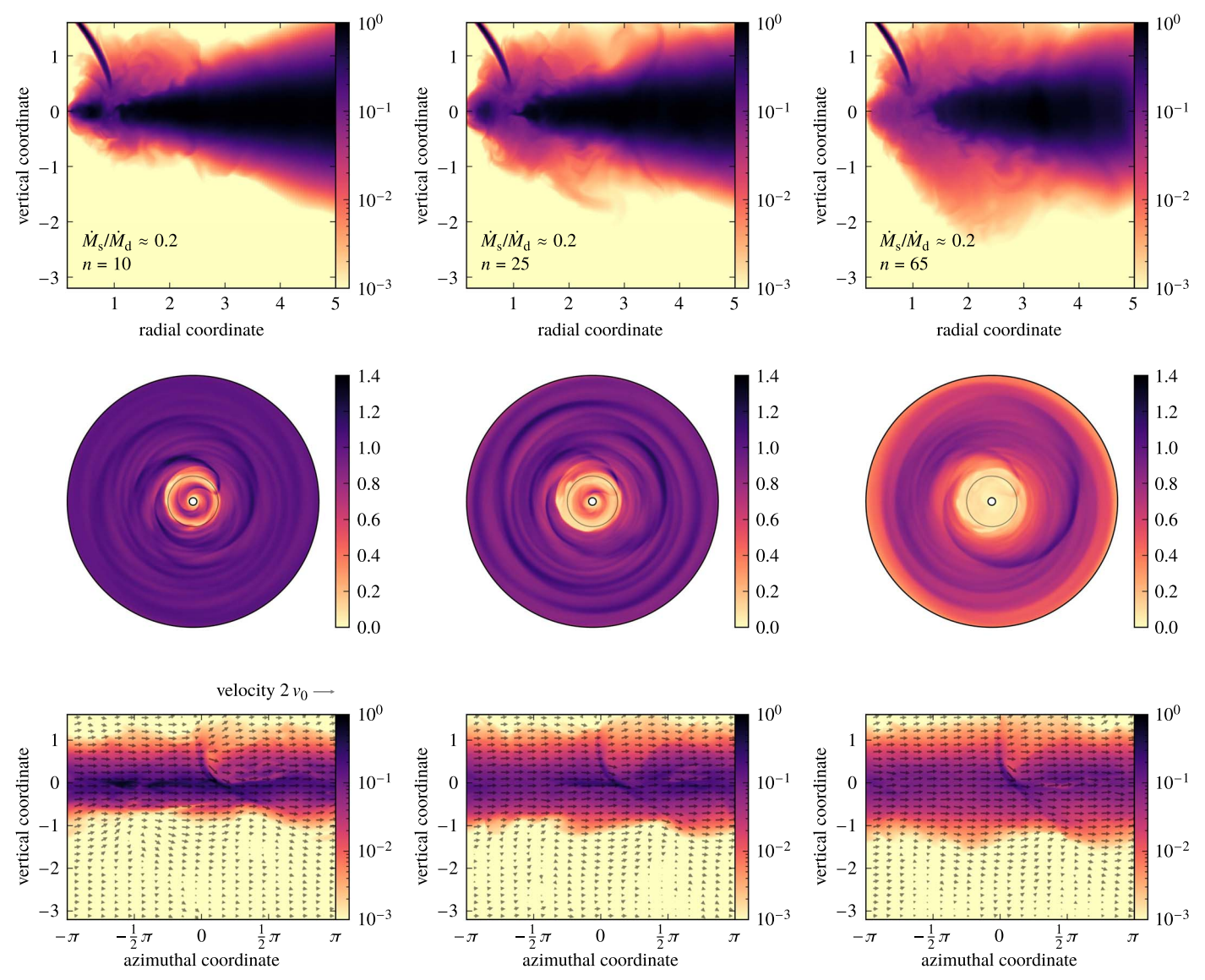


Figure 2. Orthogonal slices of the  $\dot{M}_{\rm s}/\dot{M}_{\rm d}\approx 0.2$  simulation (see movie). Each column presents one snapshot with the number n of disk orbits as indicated in the top row. The top, middle, and bottom rows are respectively a poloidal slice at  $\phi=0$ , a midplane slice, and a cylindrical slice at  $R=r_0$ . The slices intersect at  $(R, \phi, z)=(r_0, 0, 0)$ ; this is where the stream would reach pericenter if the disk were absent, and approximately where the stream collides with the disk when the disk is present. Colors plot density; the color scale is logarithmic in the top and bottom rows and linear in the middle row. The gray circle in the middle row marks  $R=r_0$ . Arrows in the bottom row show velocity; the arrow above the left panel has length  $2 v_0$ .

the black hole on gradually shrinking, tightly wound trajectories. As is evident in the bottom row, rotation departs more and more from Keplerian as gas moves inward. Gas ultimately plunges into the cutout, most of it doing so over only a small fraction of the circumference, and then into the black hole.

### 4.2.2. Mass

The spiral shocks are extremely efficient at destroying the inner disk. For a radiation-dominated,  $\dot{M}_{\rm s}/\dot{M}_{\rm d}\approx 4$  disk with our fiducial parameters (Section 3.3), the inflow rate across the inner-radial boundary given by Figure 5 is  $\sim 1.2 \times 10^3$  to  $1.2 \times 10^4$  times the unperturbed level, or  $\sim 6$  to 50 times Eddington! In effect, the coherent spiral shocks exert an extremely strong stress on the flow, leading to an inflow rate much faster than ordinary disk processes, such as correlated MHD turbulence, could cause.

For  $\dot{M}_{\rm s}/\dot{M}_{\rm d} \lesssim 0.2$ , the inflow rate has a spike at early times lasting a few disk orbits, then relaxes at late times to  $\sim \dot{M}_{\rm s}$ . For  $\dot{M}_{\rm s}/\dot{M}_{\rm d} \gtrsim 0.4$ , the inflow rate rises in the first  $\sim 1$  to 20 disk orbits, then decays gradually as the inner disk is depleted (Section 4.1); the inflow rate at  $\gtrsim 50$  disk orbits is nearly independent of  $\dot{M}_{\rm s}/\dot{M}_{\rm d}$  because the stream appears essentially as a solid obstacle to the disk, deflecting a fixed fraction of the inner disk toward the black hole every disk orbit.

For  $\dot{M}_{\rm s}/\dot{M}_{\rm d}\lesssim 1$ , the inflow rate is quasiperiodically modulated over at least part of the simulation. The quasiperiodic variation is particularly strong for  $0.1\lesssim\dot{M}_{\rm s}/\dot{M}_{\rm d}\lesssim0.2$  and is visible in the top panel throughout the simulation. This quasiperiodicity is due to the interaction between the stationary spiral shocks and some orbiting nonaxisymmetric feature, such as the lopsided outer edge of the gap (Section 4.1).

Figure 6 shows the inflow time, or the time it takes a gas packet in the inner disk to move into the cutout on its way to the black hole. Thanks to the spiral shocks, the inflow time is

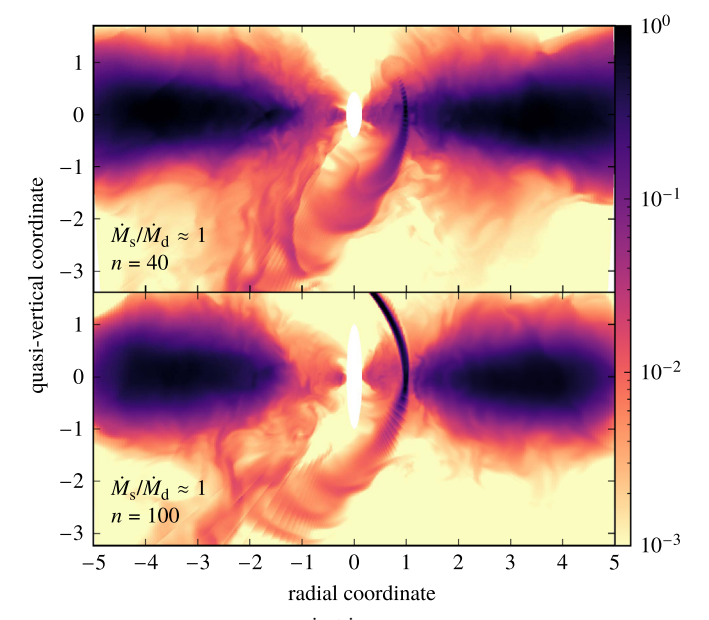


**Figure 3.** Inclined slices of the  $\dot{M}_{\rm s}/\dot{M}_{\rm d}\approx 1$  simulation. Each panel presents one snapshot with the number n of disk orbits as indicated in the bottom-left corner. Both panels are slices passing through the origin and the stream pericenter, but the top and bottom panels are rotated 0.35 rad and 0.15 rad respectively from the vertical, to match the orbital plane of the outgoing material. The stream is more strongly deflected at early times, so only at late times can we pick a slice where both the incoming stream and the outgoing material are simultaneously visible. Colors plot density.

orders of magnitude shorter than that of an unperturbed Shakura & Sunyaev (1973) disk measured at stream pericenter, which is  $\sim 1.8 \times 10^5 \, (\alpha/0.1)^{-1} [(H/R)_{\rm d}/(0.003)]^{-2}$  disk orbits, but the multistep nature of the shock-driven inflow mechanism (Section 4.2.1) means the inflow time is still at least a few disk orbits.

The inflow time is not the characteristic timescale on which the inner disk mass decreases; this is because, as we shall see in Section 4.4, the inner disk captures enough of the stream to resupply itself. Figure 7 demonstrates this considerably slower depletion of the inner disk. Although the surface density declines monotonically with time, by the end of the simulations at 100 disk orbits, which is  $\sim 0.3~T_{\rm mb}$  for our fiducial parameters (Section 3.3), the surface density is only about an order of magnitude lower than its unperturbed value. Because a radiation-dominated,  $\dot{M}_{\rm s}/\dot{M}_{\rm d}\approx 4$  disk with our fiducial parameters (Section 3.3) starts out with a Thomson optical depth of  $\sim 8000$ , it stays optically thick to electron scattering throughout the simulations.

#### 4.3. Energy Dissipation

Figure 8 tracks the time evolution of the energy dissipation rate. For a radiation-dominated,  $\dot{M}_{\rm s}/\dot{M}_{\rm d}\approx 4$  disk with our fiducial parameters (Section 3.3), the energy dissipation rate is  $\sim\!300$  to 2000 times the unperturbed disk accretion luminosity, or  $\sim\!1.5$  to 10 times the Eddington luminosity.

For  $\dot{M}_{\rm s}/\dot{M}_{\rm d} \lesssim 0.2$ , the energy dissipation rate is always close to the stream kinetic energy current; therefore, energy dissipation is well described as due to a perfectly inelastic collision between the stream and an immovable disk. For  $\dot{M}_{\rm s}/\dot{M}_{\rm d} \gtrsim 0.8$ , the energy dissipation rate initially rises but eventually falls; the energy dissipation rate shows little dependence on  $\dot{M}_{\rm s}/\dot{M}_{\rm d}$  at  $\gtrsim 15$  disk orbits. Because the disk cannot fully stop the stream in these simulations, less of the

stream kinetic energy is dissipated. Instead, the heavy stream acts as a stationary barrier to orbiting disk gas, and disk kinetic energy is dissipated when disk gas runs into the stream or the shocks created by the collision. The falloff in the energy dissipation rate over time is the result of the disk density decreasing (Section 4.1). For  $\dot{M}_{\rm s}/\dot{M}_{\rm d}\approx 0.4$  lying between the two extremes, the behavior of the energy dissipation rate switches from resembling lighter-stream simulations in the beginning to resembling heavier-stream simulations later on, suggesting that the stream takes time to clear out a gap in the disk before it can go through with little impediment.

### 4.4. Outgoing Material

The top panel of Figure 9 plots the outgoing material mass current, showing only the simulations for which the outgoing material has a mass current  $\geqslant 1\%$  that of the incoming stream throughout most of the simulation. A greater fraction of the stream passes through at later times because the disk density is lower (Section 4.1), but there are large and rapid fluctuations about the overall rising trend.

The bottom panel displays the mass current of the incoming stream stopped by the disk. For  $\dot{M}_s/\dot{M}_d \lesssim 0.2$ , the stopped mass current is  $\approx \dot{M}_s$ , which in turn is approximately the inflow rate in Figure 5. We may therefore picture the stream as being absorbed into the disk and deflected straight toward the black hole; the latter part is consistent with the fact that the disk removes all kinetic energy from lighter streams (Section 4.3). For  $\dot{M}_s/\dot{M}_d \gtrsim 0.8$ , the disk shaves off only a fraction of the incoming stream because the inner disk is cleared out early on (Section 4.2.2).

In all cases, the stopped mass current is almost always larger than the inflow rate in Figure 5. Mass loss from the inner disk (Section 4.2.2) slows down significantly if just a fraction of this mass current is diverted to resupply the inner disk. The inner disk mass still decreases over time because the outer disk receives part of the stopped mass current, because gas splashes back from the upper side of the disk, and because the collision heats up the inner disk (Section 4.1), causing it to expand out through the upper-vertical boundary or outward in radius.

Since the outgoing material is rather cold when it reaches the lower-vertical boundary, with sound speed  $\lesssim 0.1~v_0$ , its dynamics beyond the simulation domain is dictated by its mechanical energy. Figure 10 shows the specific mechanical energy distribution of the outgoing material, again only for simulations with substantial outgoing material. The most bound part has specific binding energy  $\sim 0.05~GM_h/r_0$ , hence it flies out on an elliptical orbit to  $\sim 19$  times the pericenter distance, then returns to pericenter after  $\sim 0.09~T_{\rm mb}~[M_h/(10^6M_\odot)]^{-1/2}(M_\star/M_\odot)^{1/2}(r_p/r_0)^{-3/2}$ .

Most of the outgoing material, having received a kick from the disk during the collision, is unbound with specific mechanical energy  $\sim 0.03~GM_h/r_0$ . The outgoing material carries much less energy than is dissipated in the collision (Section 4.3), but is much more energetic than the debris unbound during the initial disruption. The disk is less dense at later times (Section 4.1) and imparts a smaller force on the stream, thus the outgoing material is less and less unbound after  $\sim 40$  disk orbits.

Two caveats must be noted. First, we use a marginally bound parabolic incoming stream in the simulations, whereas a realistic incoming stream has specific binding energy  $\sim 0.01~GM_h/r_0 \times [M_h/(10^6M_\odot)]^{-1/3}(M_\star/M_\odot)^{1/3}(r_p/r_t)^{-1}$ . We therefore expect

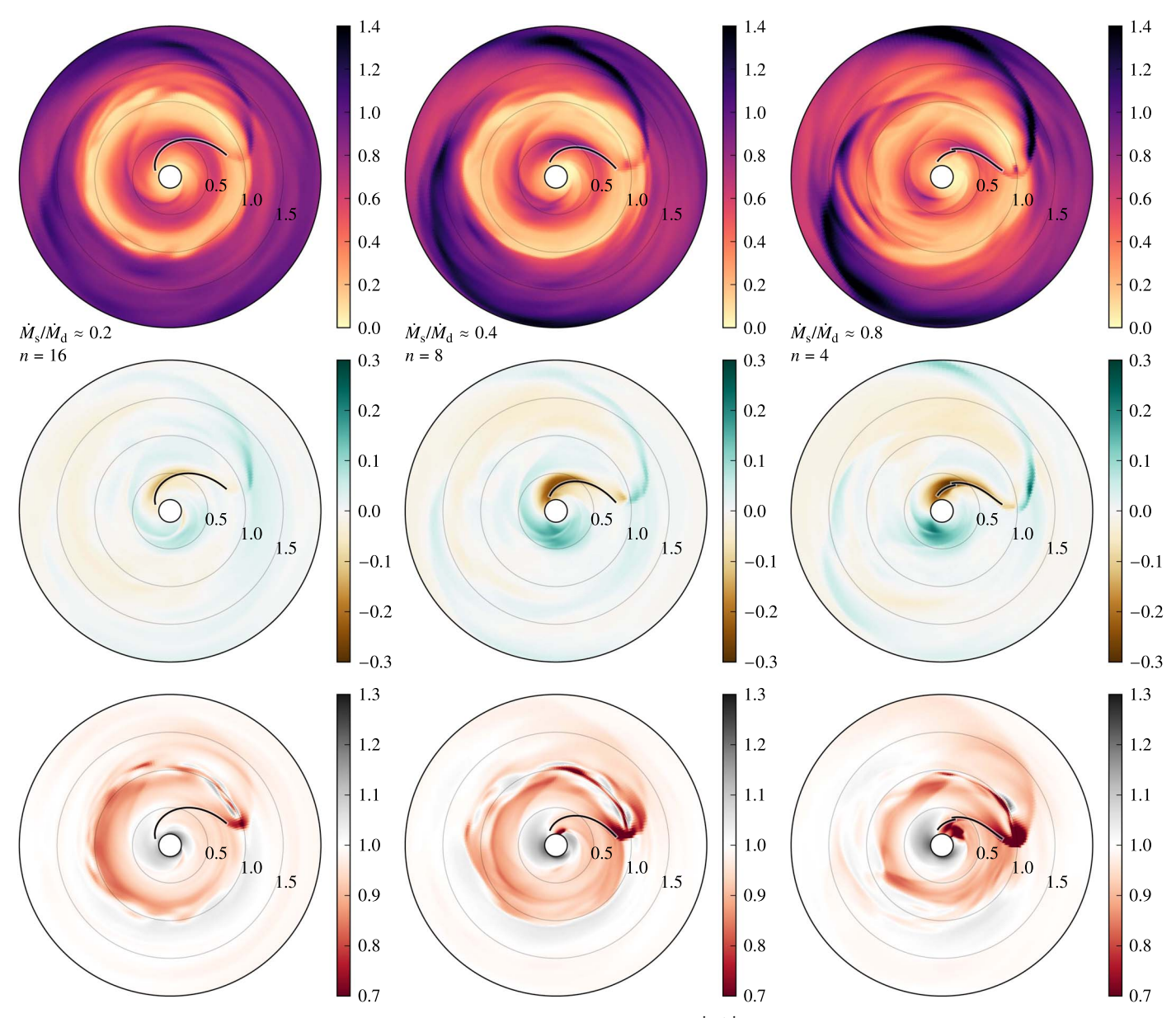


Figure 4. Zoomed-in midplane slices. Each column presents one snapshot with mass current ratio  $\dot{M}_{\rm s}/\dot{M}_{\rm d}$  and the number n of disk orbits as indicated between the top and middle rows. Colors in the top row plot density, in the middle row the radial mass flux, and in the bottom row the azimuthal velocity divided by the Keplerian orbital velocity. The black arcs above the cutout trace where the radial mass flux, the quantity plotted in the middle row, is the most strongly inward.

the specific mechanical energy distribution of realistic outgoing material to be shifted toward lower energies by a similar amount, changing the fraction of bound and unbound material. Second, the bound outgoing material may not return to pericenter if it is intercepted on the way by the large-scale disk (Kathirgamaraju et al. 2017).

### 5. Discussion

### 5.1. Timescales

TDEs in AGNs are governed by several timescales. Here we group them together in ways that allow meaningful comparisons.

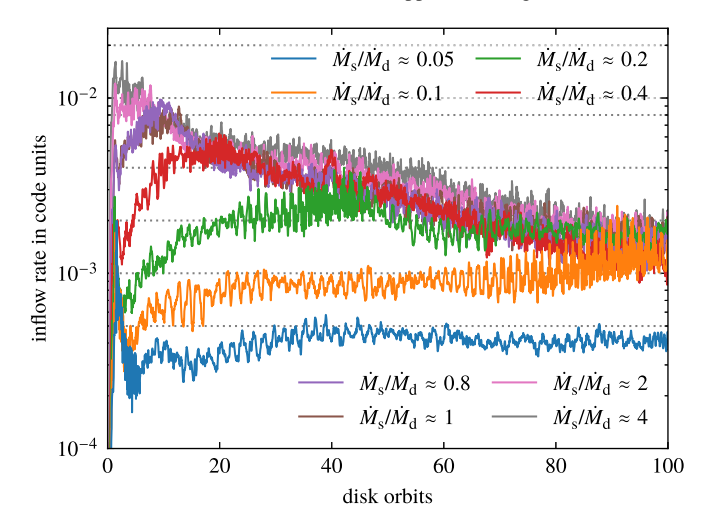
### 5.1.1. Timescales of Unperturbed Disk Flows

The shortest and longest timescales of the system both pertain to the unperturbed disk. The disk dynamical time at stream pericenter is  $1/(2\pi)$  disk orbit or  $\sim 0.018 \ days \times (M_{\star}/M_{\odot})^{-1/2} (r_{\star}/R_{\odot})^{3/2} (r_{\rm p}/r_{\rm t})^{3/2}$ . It is  $(r_{\rm p}/r_{\rm t})^{3/2}$  times the stellar dynamical time. Because outgoing waves (Section 4.1) are launched into the outer disk by the time-varying conditions near the impact point, the frequency of these waves is approximately the inverse of the disk dynamical time.

The unperturbed accretion time of a Shakura & Sunyaev (1973) disk at stream pericenter is  $\sim\!60~{\rm yr}~\times (M_\star/M_\odot)^{-1/2}$   $(r_\star/R_\odot)^{3/2}(r_{\rm p}/r_{\rm t})^{3/2}(\alpha/0.1)^{-1}[(H/R)_{\rm d}/(0.003)]^{-2}$ .

# 5.1.2. Timescales of Flows Caused by the TDE

The mass return time is given by Equation (12); in physical units, it is  $\sim 40~days \times [M_{\rm h}/(10^6 M_{\odot})]^{1/2} (M_{\star}/M_{\odot})^{-1} (r_{\star}/R_{\odot})^{3/2} (r_{\rm p}/r_{\rm t})^3$ . This is the timescale on which the incoming stream, and hence the energy dissipation rate in the collision, taper off. Because this timescale is sufficiently longer than the duration



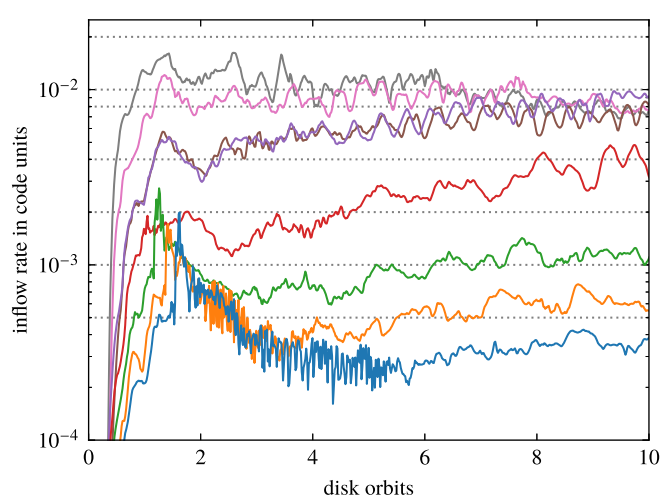


**Figure 5.** Plot of the disk-like (Section 3.4) inflow rate across the inner-radial boundary as a function of time. The code unit is  $\rho_0 r_0^2 v_0$ , where  $\rho_0$  is from Equation (16), and  $r_0$  and  $v_0$  are from Section 3.2. The top and bottom panels differ only in that the top panel looks at long-term behavior while the bottom panel zooms in on early times. The horizontal lines mark the stream mass current  $\dot{M}_s$  in ascending order from bottom to top, omitting the largest  $\dot{M}_s$ .

of our simulations, we can approximate the mass return rate to be constant.

The inflow time is the time a gas packet takes to fall toward the black hole, hence also the time over which the rest energy of the gas packet is converted to internal energy. For heavier streams, the inflow time declines slowly over time from  $\sim 1$  to  $0.5~{\rm day} \times (M_\star/M_\odot)^{-1/2} (r_\star/R_\odot)^{3/2} (r_{\rm p}/r_{\rm i})^{3/2}$ ; for the lightest stream, it decreases from  $\sim 50~{\rm to}~12~{\rm days} \times (M_\star/M_\odot)^{-1/2} (r_\star/R_\odot)^{3/2} (r_{\rm p}/r_{\rm i})^{3/2}$  (Section 4.2.2).

If the stream is heavy enough to drill through the disk, part of the outgoing material will be bound. The bound material travels on an elliptical orbit of period  $\sim$ 4 days  $\times$   $(M_{\star}/M_{\odot})^{-1/2}(r_{\star}/R_{\odot})^{3/2}(r_{\rm p}/r_{\rm t})^{3/2}$  (Section 4.4), which is considerably shorter than the mass return time. The bound material will encounter the disk a second time, but because it is much more dilute than the incoming stream (Section 4.1), this time it will simply adhere to the disk and not go through; a rise in the energy dissipation rate accompanies this interaction. As the incoming stream weakens over time and less outgoing material is ejected, this extra energy dissipation ceases as well.

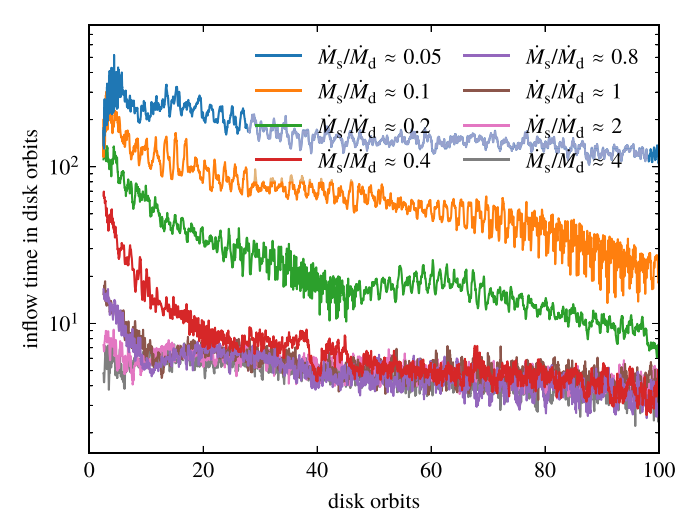


**Figure 6.** Plot of the inflow time, defined as the disk-like (Section 3.4) mass at  $R \le r_0$  divided by the disk-like inflow rate across the inner-radial boundary (Figure 5), as a function of time.

The collision leaves the disk in a very perturbed state. The disk returns to its unperturbed state when the depleted inner disk (Section 4.1) is refilled with gas from the outer disk. The timescale is very uncertain because our simulations do not take into account how magnetic stresses pull gas in. For a Shakura & Sunyaev (1973) disk, the resupply time is simply the unperturbed accretion time (Section 5.1.1). However, if gas pressure falls sharply from the outer disk to the inner, magnetic loops can stretch inward across the interface. Orbital shear then creates magnetic stresses strong enough to pull gas along with the loops, allowing gas to spiral inward over ~10 disk orbits, or  $\sim 1.2 \text{ days} \times (M_{\star}/M_{\odot})^{-1/2} (r_{\star}/R_{\odot})^{3/2} (r_{\rm p}/r_{\rm t})^{3/2}$ . Such effects are seen generically in the initial transient phase of global MHD disk simulations (Noble et al. 2011). Because the disk already captures enough mass from the stream to greatly reduce its mass loss rate (Section 4.4), even a small amount of resupply could allow the mass and surface density of the inner disk to reach steady state within a fraction of the mass return time.

#### 5.1.3. Timescales of Energy Release

The cooling time is the time it takes radiation originating from the midplane to diffuse out of the geometrically (Section 4.1) and optically (Section 4.2.2) thick inner disk; it is  $\tau_T H/c$ , where H is the height of the perturbed inner disk measured at stream pericenter. For an inner disk of aspect ratio unity, the cooling time is

$$\sim 30 \text{ days} \times \left(\frac{M_{\text{h}}}{10^6 M_{\odot}}\right)^{1/3} \left(\frac{M_{\star}}{M_{\odot}}\right)^{-1/3} \left(\frac{r_{\star}}{R_{\odot}} \frac{r_{\text{p}}}{r_{\text{t}}}\right) \left(\frac{\tau_{\text{T}}}{10^4}\right). \quad (18)$$

Here  $\tau_{\rm T}$  is the Thomson optical depth at stream pericenter (Figure 7). For a radiation-dominated,  $\dot{M}_{\rm s}/\dot{M}_{\rm d}\approx 4$  disk with our fiducial parameters (Section 3.3), the cooling time drops from  $\sim\!21$  to  $\sim\!1.4$  days over the course of  $\approx\!12$  days. The cooling time is so long because  $\tau_{\rm T}$  is  $\sim\!0.1$  times the unperturbed Thomson optical depth (Section 4.2.2) but H rises greatly due to sudden heating. How quickly  $\tau_{\rm T}$  declines depends on the amount of resupply (Section 5.1.2).

Because the inner disk is optically thick to scattering, the inflow time (Section 5.1.2) is also the time radiation has to

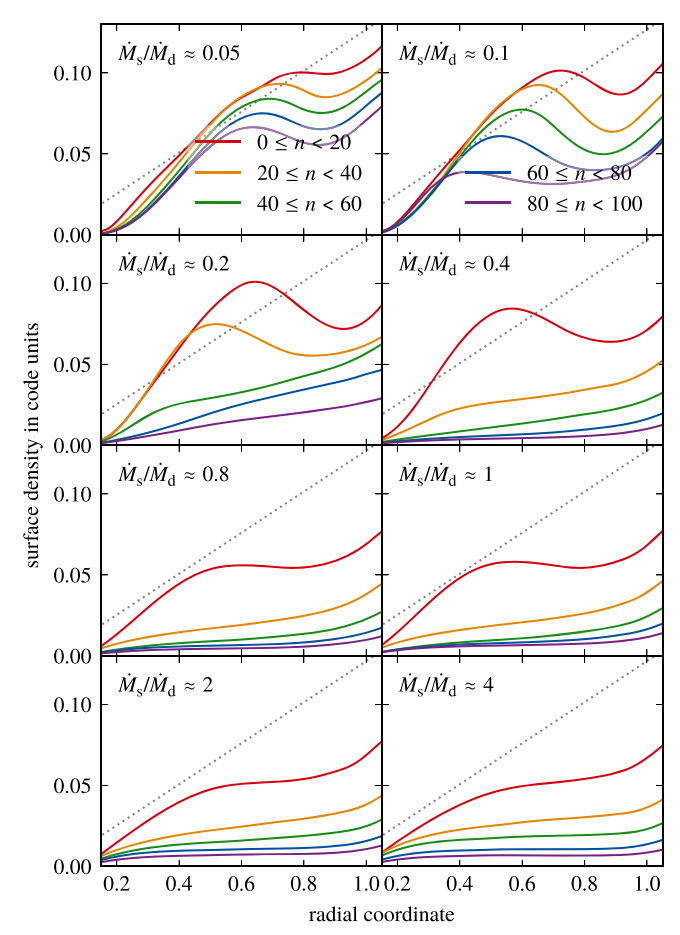


**Figure 7.** Plot of the azimuthally averaged disk-like (Section 3.4) surface density, defined as half of the integral of density from one side of the inner disk to another, as a function of radius. The code unit is  $\rho_0 r_0$ , where  $\rho_0$  is from Equation (16) and  $r_0$  is from Section 3.2. The dotted line shows the unperturbed disk surface density given by Equation (15); the colored curves are time-averages over the number n of disk orbits specified in the legend. Each panel presents one simulation with mass current ratio  $\dot{M}_{\rm s}/\dot{M}_{\rm d}$  as indicated in the top-left corner.

escape before being swallowed. The ratio of the inflow time to the cooling time is a rough estimate of the fraction of internal energy generated in the collision that is released as radiation. For a radiation-dominated,  $\dot{M}_{\rm s}/\dot{M}_{\rm d}\approx 4$  disk with our fiducial parameters (Section 3.3), the ratio rises from  $\sim\!0.06$  to  $\sim\!0.3$  over  $\approx 12$  days. Most of the energy is therefore advected into the black hole, suppressing the collision luminosity. The situation may change if the inner disk is further depleted and its optical depth diminished accordingly.

### 5.1.4. Hierarchy

For a radiation-dominated,  $\dot{M}_{\rm s}/\dot{M}_{\rm d} \approx 4$  disk with our fiducial parameters (Section 3.3), the shortest timescale is the disk dynamical time,  $\sim 0.018$  days. Next in order is the inflow time due to shocks, bottoming out at  $\sim 0.5$  to 1 day within  $\sim 1$  day from the beginning of the collision. Magnetic stresses could bring gas from the outer disk into the inner disk over  $\sim 1.2$  days, while the bound outgoing material falls back to the disk in  $\sim 4$  days. These timescales are followed by the cooling time due to radiative diffusion from the inner disk, which starts at  $\sim 21$  days but drops to  $\sim 1.4$  days within  $\approx 12$  days. Longer

still is the mass return time,  $\sim$ 40 days. The unperturbed disk accretion time,  $\sim$ 60 yr, is much longer than all of the other timescales and is therefore irrelevant.

### 5.2. Energetics

We present an inventory of the time-integrated amount of energy we may expect over the course of the entire event, including the energy from processes not directly simulated. All items except the last are concerned with internal energy production in the disk; the energy emitted as light from the disk could be much smaller because radiation could be trapped in the inflow and swallowed by the black hole (Section 5.1.3).

For lighter streams, the stream loses all of its kinetic energy at the collision (Section 4.3); its gas assimilates into the disk (Section 4.4) and moves inward to the black hole within an inflow time. The energy dissipated in this whole process is the same as if the stream were accreted directly onto the black hole, that is,  $E_{\star} \sim 9 \times 10^{52}$  erg  $\times (M_{\star}/M_{\odot})(\eta/0.1)$ . The energy dissipated may be smaller because shocks in the inner disk may send gas straight into the black hole (Section 4.2.1).

In the meantime, shocks excited by the collision inner disk (Section 4.1). The energy produced is  $E_{\rm d}\sim 6\times 10^{50}\,{\rm erg}\times [M_{\rm h}/(10^6M_\odot)]^{-1/3}(M_\star/M_\odot)^{-7/6}(r_\star/R_\odot)^{7/2}(r_{\rm p}/r_{\rm n})^{7/2}(\alpha/0.1)^{-1}(\eta/0.1)^2$  [ $(L_{\rm a}/L_{\rm E})/0.005$ ]<sup>-1</sup> for a radiation-dominated inner disk. It can be smaller if shocked gas plunges into the black hole (Section 4.2.1) or if only part of the pre-existing inner disk is accreted.

After the event is over, magnetic stresses gradually replenish the inner disk with gas from the outer disk (Section 5.1.3). Energy of order the binding energy of the unperturbed inner disk is released, which is  $E_{\rm r} \sim 9 \times 10^{49}\,{\rm erg} \times [M_{\rm h}/(10^6M_\odot)]^{1/3}(M_\star/M_\odot)^{-5/6}$   $(r_\star/R_\odot)^{5/2}(r_{\rm p}/r_{\rm l})^{5/2}(\alpha/0.1)^{-1}(\eta/0.1)[(L_{\rm a}/L_{\rm E})/0.005]^{-1}$  if the inner disk is radiation-dominated. Should magnetic stresses be strong enough to keep the inner disk refilled even while the event is in progress (Section 5.1.2), the continuous inflow of gas from the outer disk to the black hole during the event may lead to a total amount of energy dissipated exceeding  $E_{\rm d}+E_{\rm r}$ .

For heavier streams, the situation is more complicated. The inner disk is similarly flushed out by shocks, generating  $E_{\rm d}$  of internal energy in the process, and the inner disk is likewise resupplied by the outer disk, yielding  $E_{\rm r}$ . The difference is that the disk now captures only a fraction  $f_{\rm c} \sim 0.5$  of the incoming stream (Section 4.4), and the rest of the stream emerges on the other side as outgoing material. The energy available from the initial dissipation at the impact point and from the subsequent inflow of stream gas is therefore only  $\approx f_{\rm c} E_{\star}$ . The value of  $f_{\rm c}$  decreases with  $\dot{M}_{\rm s}/\dot{M}_{\rm d}$  and time, the decrease being the sharpest around  $\dot{M}_{\rm s}/\dot{M}_{\rm d} \sim 1$  (Section 4.4).

Some of the outgoing material remains bound, with a range of specific binding energy from  $\sim 0.05~GM_h/r_p$  to zero (Section 4.4). Different parts of the bound material fly out to their respective apocentric distances of  $\gtrsim 19~r_p$ , at which point they run into the disk again. Because the bound material is much more diffuse than the incoming stream was at pericenter (Section 4.1), we expect the disk to capture all of the bound material. The kinetic energy dissipated is  $\lesssim 2 \times 10^{49}~\rm erg \times (M_\star/M_\odot)^2 (r_\star/R_\odot)^{-1} (r_p/r_i)^{-3} (f_b/0.5)$ , with  $f_b \leqslant 1 - f_c$  the fraction of the incoming stream ending up in the bound material; therefore, the second collision may be too dim to be seen against the first collision and the background AGN. The captured bound material accretes along with the disk, but the

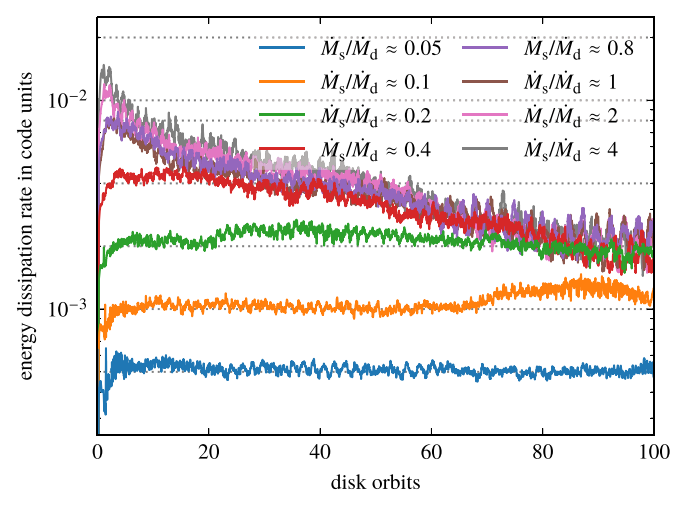


**Figure 8.** Plot of the energy dissipation rate, defined as the volume integral of  $\partial(\rho e)/\partial t + \nabla \cdot (\rho e v) + p \nabla \cdot v$  over the simulation domain, as a function of time. The code unit is  $\rho_0 r_0^2 v_0^3$ , where  $\rho_0$  is from Equation (16), and  $r_0$  and  $v_0$  are from Section 3.2. The horizontal lines mark the stream kinetic energy current for different stream mass current  $\dot{M}_s$  in ascending order from bottom to top, omitting the largest  $\dot{M}_s$ .

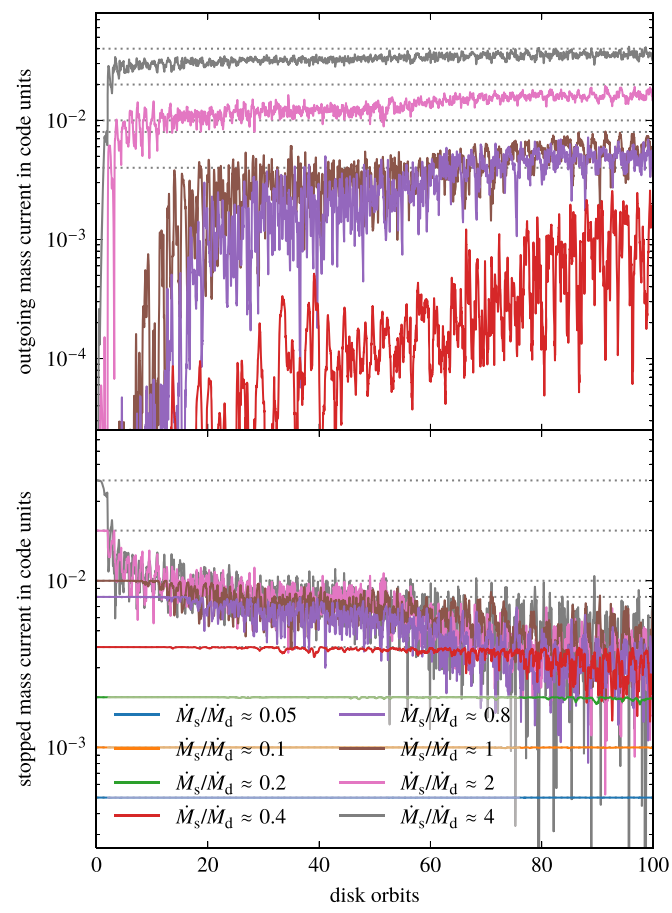


**Figure 9.** Top panel: plot of the mass current of the stream-like (Section 3.4) outgoing material emerging from the bottom of the disk as a function of time. The code unit is  $\rho_0 r_0^2 v_0$ , where  $\rho_0$  is from Equation (16), and  $r_0$  and  $v_0$  are from Section 3.2. Simulations with negligible outgoing material are hidden. The horizontal lines mark the stream mass current  $\dot{M}_s$  for the simulations shown. Bottom panel: plot of the stopped mass current, defined as  $\dot{M}_s$  minus the outgoing material mass current depicted in the top panel. The horizontal lines mark  $\dot{M}_s$  for each simulation. The stopped mass current is generally larger than the inflow rate in Figure 5, implying that the stream carries enough mass to potentially resupply the inner disk.

accretion energy can be neglected because the accretion timescale is much longer than the mass return time.

The previous paragraph pertains to the particular stream configuration used in our simulations, one where the stream plane is perpendicular to the disk plane and the stream pericenter is in the disk plane (Section 3.4). In the general case where the two planes are oriented randomly, it is more likely that the first and second collisions both occur near pericenter. Such a second collision dissipates  $\sim 5 \times 10^{51} \, \mathrm{erg} \times$  $[M_h/(10^6M_{\odot})]^{2/3}(M_{\star}/M_{\odot})^{4/3}(r_{\star}/R_{\odot})^{-1}(r_p/r_t)^{-1}(f_h/0.25)$ , much greater than if the second collision were at apocenter. This energy is a sizable fraction of that obtained by accreting the bound material directly,  $f_{\rm b}E_{\star}$ , because  $r_{\rm t}/r_{\rm g}$  is typically only a few times  $\eta^{-1}$ , according to Equation (1). The dissipation occurs over large areas of the disk and possibly at high altitudes, both of which have implications for how much of the dissipated energy would emerge as radiation. The remainder of  $f_b E_{\star}$  is liberated when the bound material falls toward the black hole.

Some of the outgoing material is unbound by a kick from the disk and carries specific kinetic energy  $\sim 0.03~GM_h/r_p$  at infinity (Section 4.4). The total energy is  $\sim 1.4 \times 10^{50} \, \mathrm{erg} \times [M_{\mathrm{h}}/(10^6 M_{\odot})]^{2/3} (M_{\star}/M_{\odot})^{4/3} (r_{\star}/R_{\odot})^{-1} (r_{\mathrm{p}}/r_{\mathrm{t}})^{-1} (f_{\mathrm{u}}/0.25)$ , where  $f_{\mathrm{u}} =$  $1 - f_{\rm c} - f_{\rm b}$  is the fraction of the incoming stream unbound by the collision. Compared to the primary ejecta unbound as an immediate consequence of the disruption (Guillochon et al. 2016; Krolik et al. 2016; Yalinewich et al. 2019), this secondary ejecta has a fraction  $\approx f_{\rm u}$  of the mass, higher velocity (Section 4.4), and a larger opening angle (Section 4.1). The ejecta drives a bow shock while running into the surrounding medium, and relativistic electrons accelerated in this shock can produce synchrotron radiation (Krolik et al. 2016; Yalinewich et al. 2019). At later times, the shock driven by the ejecta may mimic a supernova remnant (Guillochon et al. 2016). The denser medium around AGNs could mean that TDEs are more radiobright in AGNs than in vacuum. The prompt emission due to the secondary ejecta could be more luminous than the primary ejecta because the fastest material has higher velocity and a wider interaction area (Krolik et al. 2016; Yalinewich et al. 2019). All these may explain why the radio transient Cygnus A-2 (Perley et al. 2017), if interpreted as a thermal TDE happening in an AGN (de Vries et al. 2019), is brighter in radio than typical thermal TDEs in vacuum.

### 5.3. Inner Disk

#### 5.3.1. Thermodynamics

Our simulations do not correctly track temperatures because the adiabatic index used corresponds to gas pressure and not radiation pressure. To estimate the gas and radiation temperatures of the inner disk, we observe that shocks raise the sound speed of the simulated inner disk to  $\sim\!0.2$  to 0.5 times the local Keplerian orbital velocity; this corresponds to a gas temperature of

$$\sim 2 \times 10^{10} \text{ K} \times \left(\frac{M_{\rm h}}{10^6 M_{\odot}}\right)^{2/3} \left(\frac{M_{\star}}{M_{\odot}}\right)^{1/3} \left(\frac{r_{\star}}{R_{\odot}} \frac{R}{r_{\rm t}}\right)^{-1}$$
. (19)

If gas and radiation in the inner disk had enough time to thermalize, they would come into an equilibrium temperature of

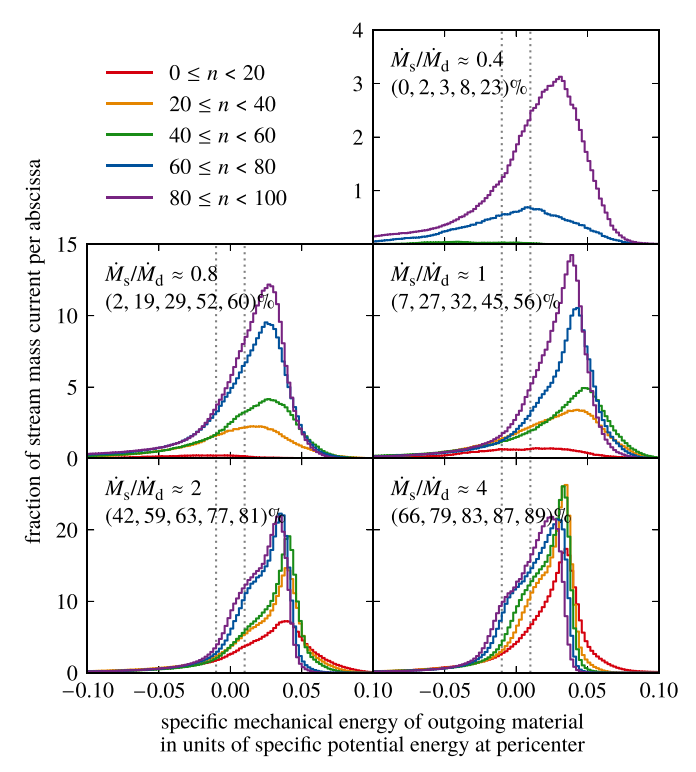


Figure 10. Histogram of the mass current-weighted specific mechanical energy of stream-like (Section 3.4) outgoing material. Each panel presents one simulation with mass current ratio  $\dot{M}_{\rm s}/\dot{M}_{\rm d}$  as indicated in the top-left corner; only simulations with the largest  $\dot{M}_{\rm s}/\dot{M}_{\rm d}$  are included. The time intervals over which the histograms are computed are given in the legend in terms of the number n of disk orbits. Each histogram is normalized such that the area under it is the fraction of the incoming stream ending up in the outgoing material; these areas are given in the top-left corner underneath  $\dot{M}_{\rm s}/\dot{M}_{\rm d}$ . Note that the ordinate range varies from row to row. The vertical lines indicate the characteristic energy spread the initial disruption imparts to the stellar material for our fiducial parameters  $M_{\rm h}=10^6M_{\odot},~M_{\star}=M_{\odot},~{\rm and}~r_{\star}=R_{\odot}$  (Section 3.3).

$$T_{\rm eq} \sim 6 \times 10^5 \,\mathrm{K} \times \left(\frac{M_{\rm h}}{10^6 M_{\odot}}\right)^{1/6} \left(\frac{M_{\star}}{M_{\odot}}\right)^{1/12} \times \left(\frac{r_{\star}}{R_{\odot}} \frac{R}{r_{\rm t}}\right)^{-1/4} \left(\frac{\rho}{2 \times 10^{-10} \mathrm{g \ cm^{-3}}}\right)^{1/4}, \tag{20}$$

where  $\rho$  is the inner disk density during the collision, and its fiducial value is the typical density at the end of the  $\dot{M}_{\rm s}/\dot{M}_{\rm d}\approx 4$  simulation for a radiation-dominated disk with our fiducial parameters (Section 3.3). In thermodynamic equilibrium, the internal energy is dominated by radiation and varies  $\propto T_{\rm eq}^4$ , hence  $T_{\rm eq}$  is rather insensitive to the specific values of the parameters on the right-hand side.

However, it may be difficult for gas raised to  $T \sim 10^{10}$  K to reach thermodynamic equilibrium. Because the cross section per mass for free–free absorption is  $\propto \rho T^{-7/2}$ , gas this hot would have essentially zero absorptivity and therefore, by Kirchhoff's law, essentially zero emissivity. The post-shock gas could cool by inverse Compton scattering off photons already present in the gas, but this, too, is problematic. The cooling rate is proportional to the local radiation energy density, which depends strongly on whether the gas originates from the colder stream or the hotter unperturbed inner disk. Even if Compton cooling is rapid, it creates no new photons, so

the temperature decrease it achieves may be limited. Substantial Compton cooling may be possible only at high latitudes, where the post-shock gas is exposed to photons radiated by the outer disk. Close to the midplane, Compton cooling may create photons energetic enough to produce pairs, which could hasten thermalization. For all these reasons, without detailed calculations, we cannot make a firm statement about how rapidly, or through what radiation mechanisms, the inner disk may approach thermodynamic equilibrium.

### 5.3.2. Radiative Transfer

The collision converts a sizable fraction of the stream kinetic energy to internal energy. For a radiation-dominated,  $\dot{M}_{\rm s}/\dot{M}_{\rm d}\approx 4$  disk with our fiducial parameters (Section 3.3), the shocks dissipate energy  $\sim\!300$  to 2000 times faster than internal stresses in the disk, corresponding to  $\sim\!1.5$  to 10 times the Eddington rate (Section 4.3). How the large amount of internal energy created translates to emission, however, is highly uncertain.

The critical comparison here is between the inflow time and the cooling time (Section 5.1.3). Since the cooling time depends on the inner disk mass, its value can be properly determined only with MHD simulations that self-consistently model the amount of resupply from the stream and the outer disk (Section 5.1.2). But if the inflow time is indeed shorter than the cooling time over a significant fraction of the mass return time, as our hydrodynamics simulations suggest, then radiative transfer in the inner disk is inherently time-dependent.

The relative shortness of the inflow time means radiation near the midplane is trapped, so energy dissipation deep inside the inner disk is completely hidden from view. The only regions that can effectively cool are those so close to the photosphere that radiation can diffuse out before being swept into the black hole; consequently, the outgoing luminosity is a small fraction of the total energy dissipation rate. Even in regions from which radiation can escape, fluctuations shorter than the local diffusion time do not imprint themselves on the light curve.

A more careful treatment calls for three-dimensional, timedependent radiative transfer calculations capable of handling the high degree of asymmetry of the system: gas near shocks is denser and hotter than gas elsewhere, and the outgoing material has high enough optical depth to partially obscure one side of the inner disk.

More radiation could escape if vertical advection, for example due to magnetic buoyancy (Jiang et al. 2014), is important in transporting radiation outward. Exploring this possibility requires time-dependent radiative MHD simulations.

The interaction among the processes above and thermalization (Section 5.3.1) may depend sensitively on the specific parameters of the system. The resulting emission may not resemble a regular TDE or AGN, and may have complex temporal and spectral behavior; different TDEs in AGNs could look entirely different.

Having laid out all these complications, we may nevertheless crudely estimate the bolometric collision luminosity  $L_{\rm c}$  as proposed in Section 5.1.3: We take the ratio  $t_{\rm infl}/t_{\rm cool}$  of inflow to cooling time to be roughly the fraction of energy that escapes as radiation, and we scale the energy dissipation rate Q (Section 4.3) by it. For heavy streams, Figure 11 shows that  $L_{\rm c}$  could be briefly very super-Eddington, then settle at a near-Eddington level. For a radiation-dominated,  $\dot{M}_{\rm s}/\dot{M}_{\rm d}\approx 4$  disk with our fiducial parameters (Section 3.3), the time to steady state is  $\sim 1$  day. The fact that  $L_{\rm c}\sim L_{\rm E}$  is not surprising in retrospect. If the inner disk had enough time to thermalize (Section 5.3.1), then it would be supported vertically against

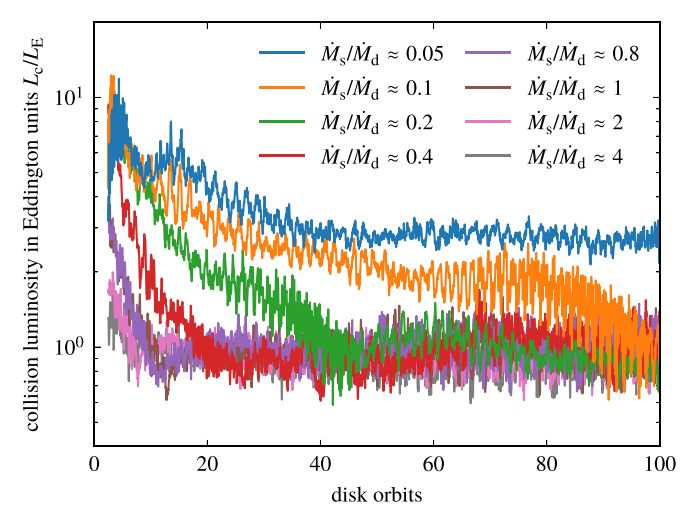


**Figure 11.** Plot of the bolometric collision luminosity  $L_{\rm c}$  in Eddington units as a function of time. The luminosity is estimated as  $L_{\rm c} \sim Q t_{\rm infl}/t_{\rm cool}$ , where Q is the energy dissipation rate (Figure 8),  $t_{\rm infl}$  is the inflow time (Figure 6), and  $t_{\rm cool}$  is the cooling time (Section 5.1.3).

gravity by radiation pressure, and the characteristic luminosity of such systems is  $L_{\rm E}$  (Krolik 2010).

### 5.4. Further Speculations

The corona of the unperturbed inner disk may be destroyed along with the inner disk itself (Section 4.1) if MHD turbulence is suppressed in the shock-driven inflow replacing it. This could explain the dip in soft X-rays lasting for a few months in the nuclear transient observed by Trakhtenbrot et al. (2019a).

The super-Eddington inflow (Section 4.2.2) may be connected to the launching of a jet (Giannios & Metzger 2011; Krolik & Piran 2012), which has been invoked to explain the hard X-ray (Bloom et al. 2011; Burrows et al. 2011; Cenko et al. 2012) and radio (van Velzen et al. 2016) emission of several TDEs. This possibility can be tested using future MHD simulations.

Acoustic waves (Section 4.1) are launched when shocks in the outer disk push orbiting gas radially outward. Bending waves are generated when the stream delivers misaligned angular momentum and exerts a torque on the disk. These waves may have observable consequences on the outer disk long after the stream has ended.

As the mass return rate dwindles toward the end of the event, the shocks would become weaker, inner-disk gas would move inward more slowly, and the gas may have enough time to completely cool off before reaching the black hole (Section 5.1.3).

## 6. Conclusions

A small fraction of TDEs is expected to take place in AGNs. As a first step toward understanding how TDEs in AGNs differ observationally from TDEs in vacuum, we have conducted a suite of simulations in which the bound debris stream of a TDE collides perpendicularly with the pre-existing accretion disk of an AGN. Our simulations show consistently that the collision creates shocks in the disk, and shocks lead to extremely super-Eddington dissipation and mass inflow rates; as a result, the disk interior to the stream impact point is heated to high temperatures and evacuated on timescales much shorter than the mass return time. Lighter streams merge with the disk, whereas heavier streams bore through; in the latter case, stream

gas shooting out of the other side of the disk may interact with the disk again or with the surrounding gas.

The parameter we vary in our simulations is  $\dot{M}_{\rm s}/\dot{M}_{\rm d}$ , the mass current carried by the stream divided by the azimuthal mass current of the disk passing under the stream footprint. It is the most important parameter governing the dynamics of the collision because it determines the relative rates at which mass, momentum, and kinetic energy are brought to the impact point by the stream and the disk. As the Eddington ratio of the AGN rises at fixed black hole mass,  $\dot{M}_{\rm s}/\dot{M}_{\rm d}$  decreases to a minimum and then increases; any given value of  $\dot{M}_{\rm s}/\dot{M}_{\rm d}$  above the minimum can be achieved in either a weakly accreting, gasdominated disk or a strongly accreting, radiation-dominated disk. Typical TDEs in AGNs have  $\dot{M}_{\rm s}/\dot{M}_{\rm d}\gtrsim 1$ .

A light stream with small  $\dot{M}_{\rm s}/\dot{M}_{\rm d}$  is completely absorbed by the disk and deflected toward the black hole. A heavy stream with large  $\dot{M}_{\rm s}/\dot{M}_{\rm d}$  penetrates the disk, shooting out fluffy outgoing material on the other side. Part of the outgoing material remains bound; it runs into the disk again eventually, this time settling onto the disk instead of punching through because its density is much lower than before. Part of the outgoing material is unbound by a kick from the disk; it escapes and interacts with the surrounding gas. All these interactions are potential energy sources for emission.

The collision dissipates mostly the kinetic energy of the stream when the stream is light, but mostly that of the disk when the stream is heavy. The internal energy, generated at a super-Eddington rate several orders of magnitude above that of the unperturbed disk, raises the aspect ratio of the inner disk to order unity.

The collision excites multiple shocks in the inner disk. Repeated encounters with shocks remove angular momentum from disk gas, causing it to move speedily inward. Heavier streams create stronger shocks, so much so that the inflow rate is enhanced to super-Eddington values orders of magnitude above that of the unperturbed disk.

Rapid inflow drains the inner disk; meanwhile, the disk replenishes itself by capturing part of the incoming stream. The net effect is still a monotonic decline of the mass and surface density of the inner disk over time, but much slower than if the stream were not captured. For heavier streams, the surface density is lowered by an order of magnitude within a fraction of the mass return time. Resupply from the outer disk due to magnetic stresses, not considered in our simulations, could help the inner disk achieve mass balance within the mass return time.

The super-Eddington inflow and energy dissipation rate does not automatically imply super-Eddington luminosity. Because the inner disk flows inward faster than radiation can diffuse out of it, only a small fraction of the energy dissipated in the collision escapes as radiation, and the rest is advected inward to the black hole. Nevertheless, the high rate at which kinetic energy is dissipated means the bolometric luminosity may be near-Eddington. It is uncertain in which energy band the radiation emerges; the spectrum could be far from thermal and may not look like a standard TDE or AGN at all. Because the inflow time is short and the density distribution has a complex geometry, robust observational predictions demand more careful treatment of the three-dimensional, time-dependent radiative transfer and the thermal evolution of the post-shock gas.

We do not know how soon the disk returns to the unperturbed state once the stream has ended; it could take decades if inflow is controlled by MHD turbulence in the usual way, or a much shorter time if the cavity interior to the impact point permits more coherent magnetic stresses to act, as often seen in MHD simulations.

We caution that, as a first step toward understanding how TDEs behave in AGNs, our simulations considered a very restricted section of the parameter space. The properties of the system as a function of time may depend on such detailed parameters as the geometry and orientation of the stream relative to the disk, the density and velocity structure of the stream, and the properties of the unperturbed disk. Moreover, our simulations did not run long enough to study what happens when the mass return rate has fallen significantly, nor did they have the ability to follow the radiative and MHD properties of the stream and the disk. The exploration of the vast parameter space and the wide range of physics will, no doubt, be the subject of future work.

The authors thank Almog Yalinewich and Nicholas Stone for insightful discussions. C.H.C. and T.P. are supported by ERC advanced grant "TReX" and the CHE-ISF Center for Excellence in Astrophysics. This work was partially supported by NSF grant AST-1715032 and by Simons Foundation grant 559794 (J.H.K.).

*Software:* Athena++ (Stone et al. 2008), Python, NumPy, h5py, Matplotlib, VisIt, FFmpeg.

#### ORCID iDs

Chi-Ho Chan https://orcid.org/0000-0001-5949-6109
Tsvi Piran https://orcid.org/0000-0002-7964-5420
Julian H. Krolik https://orcid.org/0000-0002-2995-7717
Dekel Saban https://orcid.org/0000-0002-0350-7419

#### References

Auchettl, K., Ramirez-Ruiz, E., & Guillochon, J. 2018, ApJ, 852, 37 Blanchard, P. K., Nicholl, M., Berger, E., et al. 2017, ApJ, 843, 106 Bloom, J. S., Giannios, D., Metzger, B. D., et al. 2011, Sci, 333, 203 Bonnerot, C., Rossi, E. M., & Lodato, G. 2016, MNRAS, 458, 3324

```
Burrows, D. N., Kennea, J. A., Ghisellini, G., et al. 2011, Natur, 476, 421
Campana, S., Mainetti, D., Colpi, M., et al. 2015, A&A, 581, A17
Cenko, S. B., Krimm, H. A., Horesh, A., et al. 2012, ApJ, 753, 77
Dai, L., McKinney, J. C., & Miller, M. C. 2015, ApJL, 812, L39
de Vries, M. N., Wise, M. W., Nulsen, P. E. J., et al. 2019, MNRAS, 486, 3388
Giannios, D., & Metzger, B. D. 2011, MNRAS, 416, 2102
Grupe, D., Komossa, S., & Saxton, R. 2015, ApJL, 803, L28
Guillochon, J., McCourt, M., Chen, X., Johnson, M. D., & Berger, E. 2016,
   ApJ, 822, 48
Hills, J. G. 1975, Natur, 254, 295
Jiang, Y.-F., Stone, J. M., & Davis, S. W. 2014, ApJ, 796, 106
Kankare, E., Kotak, R., Mattila, S., et al. 2017, NatAs, 1, 865
Karas, V., & Šubr, L. 2007, A&A, 470, 11
Kathirgamaraju, A., Barniol Duran, R., & Giannios, D. 2017, MNRAS,
Kennedy, G. F., Meiron, Y., Shukirgaliyev, B., et al. 2016, MNRAS, 460, 240
Kochanek, C. S. 1994, ApJ, 422, 508
Komossa, S. 2015, JHEAp, 7, 148
Krolik, J., Piran, T., Svirski, G., & Cheng, R. M. 2016, ApJ, 827, 127
Krolik, J. H. 2010, ApJ, 709, 774
Krolik, J. H., & Piran, T. 2012, ApJ, 749, 92
Lin, D., Godet, O., Ho, L. C., et al. 2017, MNRAS, 468, 783
Mattila, S., Pérez-Torres, M., Efstathiou, A., et al. 2018, Sci, 361, 482
Merloni, A., Dwelly, T., Salvato, M., et al. 2015, MNRAS, 452, 69
Noble, S. C., Krolik, J. H., Schnittman, J. D., & Hawley, J. F. 2011, ApJ,
  743, 115
Perley, D. A., Perley, R. A., Dhawan, V., & Carilli, C. L. 2017, ApJ, 841, 117
Piran, T., Svirski, G., Krolik, J., Cheng, R. M., & Shiokawa, H. 2015, ApJ,
Rees, M. J. 1988, Natur, 333, 523
Saxton, R. D., Motta, S. E., Komossa, S., & Read, A. M. 2015, MNRAS,
  454, 2798
Shakura, N. I., & Sunyaev, R. A. 1973, A&A, 24, 337
Shiokawa, H., Krolik, J. H., Cheng, R. M., Piran, T., & Noble, S. C. 2015, ApJ,
Shu, X. W., Wang, S. S., Dou, L. M., et al. 2018, ApJL, 857, L16
Stone, J. M., Gardiner, T. A., Teuben, P., Hawley, J. F., & Simon, J. B. 2008,
    pJS, 178, 137
Trakhtenbrot, B., Arcavi, I., MacLeod, C. L., et al. 2019a, arXiv:1903.11084
Trakhtenbrot, B., Arcavi, I., Ricci, C., et al. 2019b, NatAs, 3, 242
van Velzen, S., Anderson, G. E., Stone, N. C., et al. 2016, Sci, 351, 62
Wyrzykowski, Ł., Zieliński, M., Kostrzewa-Rutkowska, Z., et al. 2017,
     NRAS, 465, L114
Yalinewich, A., Steinberg, E., Piran, T., & Krolik, J. H. 2019, MNRAS,
  487, 4083
```